Electrostatically Engineered CNT and Cross-Linked PEDOT:PSS on Mulberry Paper-Based Flexible Supercapacitor for High Electrochemical

Citation for the original published paper (version of record):
Yoon, H., Aguilo-Aguayo, N., Brette Mortensen, M. et al (2026). Electrostatically Engineered CNT and Cross-Linked PEDOT:PSS on Mulberry Paper-Based Flexible Supercapacitor for High Electrochemical Performance and Reliability. International Journal of Energy Research, 2026(1). http://dx.doi.org/10.1155/er/2065012

International Journal of Energy Research

WILEY

RESEARCH ARTICLE OPEN ACCESS

Electrostatically Engineered CNT and Cross-Linked PEDOT:PSS on Mulberry Paper–Based Flexible Supercapacitor for High Electrochemical Performance and Reliability

Hyungsub Yoon[1] | Noemí Aguiló-Aguayo[2] | Mathis Mortensen Brette[3] | Ho-Jin Lee[4] | Tung Pham[2] | Ji-Won Jung[4,5] | Peter Baumli[6] | Ergang Wang[3] | Tae Gwang Yun[7] | Byungil Hwang[8]

[1]Department of Intelligent Semiconductor Engineering, Chung-Ang University, Seoul 06974, Republic of Korea | [2]Research Institute of Textile Chemistry and Textile Physics, University of Innsbruck, Hoechsterstrasse 73, Dornbirn 6850, Austria | [3]Department of Chemistry and Chemical Engineering, Chalmers University of Technology, Göteborg 41296, Sweden | [4]Advanced Materials Program, Department of Materials Science and Engineering, Konkuk University, 120 Neungdong-ro, Gwangjin-gu, Seoul 05029, Republic of Korea | [5]Department of Materials Science and Engineering, Konkuk University, 120 Neungdong-ro, Gwangjin-gu, Seoul 05029, Republic of Korea | [6]Institute of Metallurgy, Metal Forming and Nanotechnology, University of Miskolc, Miskolc 3515, Hungary | [7]Department of Molecular Science and Technology, Ajou University, Suwon 16499, Republic of Korea | [8]School of Integrative Engineering, Chung-Ang University, Seoul 06974, Republic of Korea

Correspondence: Ergang Wang (ergang@chalmers.se) | Tae Gwang Yun (ytk0402@ajou.ac.kr) | Byungil Hwang (bihwang@cau.ac.kr)

Received: 29 October 2025 | **Revised:** 25 February 2026 | **Accepted:** 13 March 2026

Academic Editor: Weixin Guan

Keywords: carbon nanotube | cross-linking agent | flexible supercapacitor | mulberry paper | PEDOT:PSS | surfactant

ABSTRACT

The growing demand for flexible and wearable energy storage systems calls for sustainable and mechanically robust substrates that overcome the limitations of conventional rigid and nonbiocompatible materials. Here, we present a binder-free and flexible supercapacitor fabricated on mulberry paper, integrating electrostatically engineered carbon nanotubes (CNTs) and covalently cross-linked poly(3,4-ethylenedioxythiophene):poly(styrene sulfonate) (PEDOT:PSS). CNTs modified with a cationic surfactant, cetyltrimethylammonium bromide (CTAB), uniformly adhere to the hydroxyl-rich fibers via electrostatic interactions, enhancing interfacial stability and minimizing resistance. PEDOT:PSS is cross-linked using divinyl sulfone (DVS), simultaneously improving electrical conductivity and aqueous stability. The resulting device exhibits an areal capacitance of 30.4 mF cm^{-2} at 50 mV s^{-1} and maintains 95.9% of its capacitance over 80,000 cycles at 4.0 mA cm^{-2}. This study provides a scalable and low-cost platform for high-performance, durable, and flexible energy storage, highlighting a novel interfacial engineering strategy for natural fiber substrates.

1 | Introduction

The rapidly increasing global energy demand, coupled with growing interest in sustainable energy systems, underscores the urgent need for next-generation energy storage devices. The proliferation of portable electronics, wearable devices, and Internet of Things (IoT) technologies requires the development of materials that combine flexibility, lightweight characteristics, and environmental sustainability [1–5]. In this context, cellulose has attracted significant attention as a sustainable material due to its abundance, excellent biocompatibility, and biodegradability. When processed into nanofibers, cellulose provides a high surface area and porous structure, enhancing electron and ion transport and maximizing electrochemical performance, thereby overcoming the limitations of conventional metal- or polymer-based electrodes [6–8]. However, practical applications are still hindered by low electrical conductivity, limited mechanical robustness, and challenges in scalable fabrication.

Conventional approaches for Hanji-based supercapacitors primarily rely on aqueous solution processes, in which conductive carbon materials are coated onto large-area cellulose fibers [8, 9]. This enables relatively strong interfacial adhesion through van der Waals forces and π–π interactions, allowing stable attachment of conductive materials on the fiber surface [10, 11]. Nevertheless, the intrinsic hydrophobicity of carbon materials leads to poor dispersion in aqueous solutions and local aggregation, resulting in nonuniform coatings that compromise electron/ion transport and electrochemical performance [12]. Although anionic surfactants (e.g., sodium dodecylbenzenesulfonate [SDBS]) have been used to improve dispersion, their limited interfacial affinity restricts long-term coating stability and prevents optimal distribution of active materials and electrolyte infiltration, posing challenges for large-area and high-performance electrodes. Therefore, to overcome the limitations of conventional aqueous-based processes, it is essential to develop new strategies that improve the surface properties of conductive carbon materials and reinforce interfacial bonding with fibers, thereby enabling uniform coating, stable electrode architectures, and optimized electrochemical performance simultaneously.

To address these challenges, we developed a binder-free and flexible supercapacitor on mulberry paper, integrating electrostatically engineered CNT adhesion and covalently cross-linked poly(3,4-ethylenedioxythiophene):poly(styrene sulfonate) (PEDOT:PSS). Carbon nanotubes (CNTs) serve as electric double layer (EDL)-type materials but tend to aggregate due to hydrophobicity and strong van der Waals and π–π interactions [13]. To overcome this, CNTs were modified with cetyltrimethylammonium bromide (CTAB), a cationic surfactant that promotes electrostatic interaction with the negatively charged, hydroxyl-rich surface of mulberry paper, ensuring uniform coating and robust interfacial adhesion. For pseudocapacitive energy storage, PEDOT:PSS was introduced; its reversible redox reaction with the electrolyte enhances energy storage performance. However, PEDOT:PSS exhibits low aqueous stability and substrate delamination, compromising cycling stability [14]. This was addressed by divinyl sulfone (DVS) cross-linking, which forms covalent bonds with PSS chains to enhance aqueous stability and simultaneously acts as a secondary dopant to remove excess insulating PSS, improving electrical conductivity [15, 16]. By integrating CNTs and PEDOT:PSS within a single device architecture, CNTs provide rapid charge storage, while PEDOT:PSS contributes pseudocapacitance. The excellent mechanical durability and hydrophilic, porous network of mulberry paper enable the realization of a flexible supercapacitor with high power and energy densities.

2 | Materials and Methods

2.1 | Materials

All chemicals were used without further purification. Commercially available mulberry paper (thickness: 0.35 mm) was purchased from Song-jeong art supplies store. CNT was obtained from JEIO. Surfactants used included SDBS (Sigma–Aldrich) and CTAB (Daejung). PEDOT:PSS was purchased from Sigma–Aldrich. EG (Samchun Chemical) and DVS (Sejin CI Co. Ltd.) were used as cross-linking agents. Sulfuric acid (H_2SO_4) was purchased from Daejung. Sodium sulfate (Na_2SO_4) was purchased from Sigma-Aldrich.

2.2 | Preparation of the Mulberry Paper–Based Supercapacitor

To prepare CNT dispersions with SDBS or CTAB surfactants, 0.04 g of CNT, 0.04 g of surfactant, and 16 mL of deionized (DI) water were mixed and tip-sonicated for 30 min. A 12 mm diameter mulberry paper disc was then immersed in the CNT/SDBS or CNT/CTAB dispersion for 30 s, followed by drying at 80°C for 30 min in a vacuum oven. This coating process was repeated three times to ensure uniform CNT deposition on the mulberry paper. The resulting samples were denoted as CNT/CTAB and CNT/SDBS electrode, where, without any special explanation, the CNT-to-surfactant mass ratio was fixed at 1:1. Next, PEDOT:PSS aqueous dispersions were prepared using different cross-linking agents (DVS or EG). To obtain PEDOT:PSS-DVS and PEDOT:PSS-EG dispersions, 3 vol% of DVS or EG was added to PEDOT:PSS aqueous solution and stirred with a magnetic stirrer at 300 rpm for 30 min. The CNT/CTAB–coated mulberry papers were subsequently dipped into three types of PEDOT:PSS dispersions, that is, pristine PEDOT:PSS, PEDOT:PSS-DVS, and PEDOT:PSS-EG, for 30 s and dried at 80°C for 30 min in a vacuum oven. The resulting samples were denoted as C-PEDOT:PSS, C-PEDOT:PSS-DVS, and C-PEDOT:PSS-EG, respectively.

2.3 | Electrochemical Characterization

For all electrochemical measurements, 2032 coin-type cells were assembled with symmetric electrodes (12 mm diameter), 1 M H_2SO_4 as the electrolyte, and a polyethylene separator. Tests were performed over a voltage window of 0–0.85 V using a battery test system (BCS-805, BioLogic). Cyclic voltammetry (CV), galvanostatic charge–discharge (GCD), and electrochemical impedance spectroscopy (EIS) were conducted sequentially. CV curves were recorded at scan rates of 5, 10, 20, 50, 100, and 200 $\mathrm{mV\,s^{-1}}$. GCD profiles were obtained at areal current densities of 0.1, 0.2, 0.3, 0.5, and 1.0 $\mathrm{mA\,cm^{-2}}$. EIS spectra were collected from 10 kHz to 100 mHz with an applied amplitude of 10 mV. Long-term cycling was evaluated at 1.0 and 4.0 $\mathrm{mA\,cm^{-2}}$ under room temperature (25°C) and 50% relative humidity. Areal capacitance (C_a) was calculated from CV and GCD data using Equations (1) and (2), respectively. In these equations, $\int ivdv$ is the integrated CV area, μ is a scan rate, A is the area of the electrode, ΔV is the voltage window, i/A denotes the areal current density, and t is the discharge time:

$$C_a = \int \frac{ivdv}{2\mu A\Delta V}\,. \tag{1}$$

$$C_a = \frac{it}{A\Delta V}\,. \tag{2}$$

2.4 | Physical and Chemical Characterization

The surface charge of the mulberry paper and CNT dispersions was analyzed using zeta potential measurement. For the mulberry paper, the paper was cut to dimensions of 15 mm × 35 mm (~80 mg) and mounted in the clamping cell (Cat. Number 165260) of the zeta potential analyzer (SurPASS 3, Anton Paar GmbH, Graz, Austria). A streaming solution composed of 1 mM KCl and 1 mM KOH in demineralized water was used, initiating the measurement at an alkaline pH of 11. Titration was then performed by gradually adding 0.05 M HCl to generate a zeta potential vs. pH curve. The titration step size was adjusted to produce a pH change of 0.5 units per step. At each pH value, three zeta potential measurements were recorded over a streaming pressure range of 800–200 mbar. All measurements were conducted with the solution continuously degassed by nitrogen bubbling. The zeta potential of CNT dispersions was measured with a Delsa Nano C particle analyzer (Beckman Coulter) to determine the surface charge of CNT dispersions prepared with SDBS or CTAB; the CNT-to-surfactant mass ratio was fixed at 1:1. Fourier-transform infrared (FTIR) spectra were collected on an Alpha II spectrometer (Bruker) over 400–4000 cm^{-1}. X-ray photoelectron spectroscopy (XPS, K-alpha+, Thermo Fisher Scientific; Al–Kα source) was used to analyze the elemental composition (C, N, O, S, and Br) of CNT–coated mulberry papers and to quantify surface PSS content on PEDOT:PSS–coated samples after adding cross-linking agents. Surface morphology was examined with a field-emission scanning electron microscope (FE-SEM, SIGMA 300, Carl Zeiss AG). Energy dispersive X-ray spectroscopy (EDS) was conducted to examine elemental mapping of CNT–coated electrodes. Static contact angles were measured using a DSA-100 drop-shape analyzer (KRÜSS). The tensile stress–strain curves of the electrodes were measured to examine the mechanical properties (compac-100II, Sun Scientific).

3 | Results and Discussion

A binder-free and flexible supercapacitor was fabricated on mulberry paper using sequential coating of CNT and PEDOT:PSS, as illustrated in Figure 1a. To optimize CNT adhesion, we compared two types of surfactants—CTAB (cationic) and SDBS (anionic)—to examine how electrostatic interaction influences coating behavior and interfacial resistance on the negatively charged paper substrates. CNTs were dispersed with each surfactant (1:1 *w*/*w*), dip-coated onto mulberry paper, and vacuum-dried. The CNT/CTAB–coated paper, exhibiting stronger interfacial adhesion, was selected for further modification with PEDOT:PSS. To improve the aqueous stability and conductivity of the PEDOT:PSS layer, we compared two cross-linking agents—DVS (covalent bonding) and EG (hydrogen bonding)—to assess how the binding mechanism influences long-term electrochemical performance. The effects of surfactant type and cross-linking chemistry on coating uniformity, surface characteristics, and electrochemical behavior were systematically investigated.

Figure 1b–f investigates the interfacial interaction between CNT dispersions and mulberry paper depending on surfactant type. Table S1 shows the zeta potential data of the pristine mulberry paper at various pH values from 2.05 to 10.93. Zeta potential measurements confirmed that the pristine mulberry paper surface was negatively charged at various pH values from 2.53 to 10.93, due to abundant carbonyl and hydroxyl groups (Figure S1) [17]. Especially, at pH value of 6.94, the mulberry paper showed the zeta potential value of −9.68 mV, whereas CNT dispersions stabilized with CTAB (cationic) and SDBS (anionic) exhibited positive (+55.1 mV) and negative (−43.8 mV) values, respectively (Figure 1b). These results indicate favorable electrostatic attraction between CNT/CTAB and mulberry paper, supporting enhanced adhesion and uniformity. Furthermore, the absolute zeta potential value of CNT/CTAB dispersion was also higher than that of CNT/SDBS dispersion, suggesting that CNTs stabilized with CTAB were better dispersed in DI water than those stabilized by SDBS. Contact angle measurements further supported this trend. Owing to the opposite surface charges of CNT/CTAB dispersion and the mulberry paper, electrostatic attraction occurs between the dispersion and substrate, enhancing the spreading of the CNT/CTAB droplet on the paper [18, 19]. As a result, the CNT/CTAB dispersion exhibited a lower contact angle (88°) than the CNT/SDBS dispersion (101°) on mulberry paper (Figure 1c), indicating better wettability [20, 21]. This improved wettability and binding strength between CNT/CTAB and the mulberry paper facilitate the formation of a more uniform and tightly bonded CNT layer on the substrate [22–26]. Figure S2 describes coating behavior and electrical resistance over multiple cycles. After the first coating, the CNT/CTAB electrode exhibited a higher mass gain (0.32 mg) than the CNT/SDBS electrode (0.24 mg), along with lower sheet resistance (0.31 kΩ vs. 0.39 kΩ), indicating effective CNT deposition driven by electrostatic attraction. After three coatings, the mass converged to 0.86 mg for CNT/CTAB and 0.88 mg for CNT/SDBS. Notably, despite the slightly lower loading mass, CNT/CTAB electrode maintained a lower electrical resistance (0.1 kΩ) than the CNT/SDBS electrode (0.12 kΩ). Beyond the third cycle, negligible changes in mass and resistance were observed, suggesting that three coating cycles represent the optimal condition for further experiments. We summarized loading mass and electrical resistance of CNT/CTAB and CNT/SDBS electrodes depending on coating cycles in Table S2. These results demonstrate that CTAB is a more effective surfactant than SDBS for forming low-resistance CNT networks on mulberry paper using a minimal amount of CNTs. XPS analysis confirmed the presence of the surfactant-derived chemical composition on the coated mulberry papers (Figure 1d). No Br 3d or S 2p peaks were observed in pristine mulberry paper, whereas Br 3d and S 2p signals were clearly detected in CNT/CTAB– and CNT/SDBS–coated mulberry papers, respectively (Figure 1e,f). Figures S3 and S4 present SEM and EDS results, which further validate the uniform distribution of CNTs without visible aggregation, as well as the well-distributed Br and S elements in CNT/CTAB– and CNT/SDBS–coated papers, respectively. Figure S5 describes the stress-train curves of the pristine mulberry paper, CNT/CTAB, and CNT/SDBS electrodes. As shown in Figure S5, CNT/CTAB electrode exhibited the highest tensile strength (12.3 MPa), compared to the CNT/SDBS electrode (11.1 MPa) and the pristine mulberry paper (10.1 MPa). This suggests that the electrostatic attraction between positively charged CNT/CTAB and negatively charged mulberry paper fibers enhances the interfacial bonding, which is beneficial for reinforcing the mechanical strength. These results confirm the formation of a continuous and conductive CNT network—especially in the CTAB-coated sample—which is crucial for efficient charge transport and overall device performance.

The wettability of the electrode toward the electrolyte is a critical parameter in energy storage systems, as it directly affects interfacial ion transport. To evaluate this property, we measured the contact angle by dropping 1 M H_2SO_4 electrolyte onto the CNT/CTAB and CNT/SDBS electrodes (Figure S6). The contact angle of the electrolyte on the CNT/CTAB electrode was 81°, whereas that on the CNT/SDBS electrode was 92°, indicating better wettability of the CNT/CTAB surface. This enhanced wettability is expected to facilitate the improved charge transfer kinetics and overall electrochemical performance [27, 28]. To evaluate the influence of surfactant choice on the electrochemical behavior of CNT-coated electrodes, we performed EIS, CV, GCD, and cycling tests. Figure 2a describes the EIS results of CNT/CTAB and CNT/SDBS electrodes. The R_{ct} of CNT/CTAB electrode was 13.2 Ω, whereas that of CNT/SDBS was 20.9 Ω. The lower R_{ct} of CNT/CTAB electrode was attributed to the enhanced electronic transport and ion accessibility afforded by a more uniform and tightly bound CNT network and higher electrolyte wettability. The GCD profiles at 0.2 mA cm^{-2} show a longer discharge time for the CTAB–based device, indicating a higher areal capacitance (Figure 2b). Consistently, at 50 mV s^{-1}, the CV curve of the CNT/CTAB electrode encloses a larger area than that of CNT/SDBS electrode (Figure 2c). This trend persists across various current densities and scan rates (Figures S7 and S8). The areal capacitance plot further confirms superior performance of the CNT/CTAB electrode over the range of 5–200 mV s^{-1} (Figure 2d). Specifically, at 50 mV s^{-1}, the CNT/CTAB electrode delivers an areal capacitance of 10.3 mF cm^{-2}, outperforming CNT/SDBS electrode (9.3 mF cm^{-2}). Particularly noteworthy is the redox-like feature around approximately 0.8 V in the CV curve of CNT/CTAB electrode, which is absent in CNT/SDBS electrode. This feature is attributed to Br ion–based redox processes at the electrode/electrolyte interface, since CTAB contains bromide ions as counter ions. Previous studies on bromide redox-active electrolytes with carbon- and CNT–based electrodes

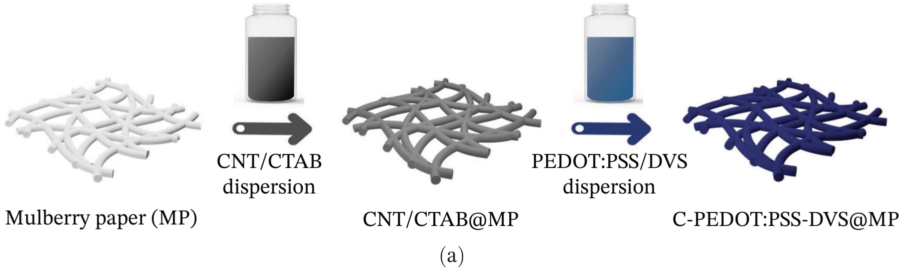

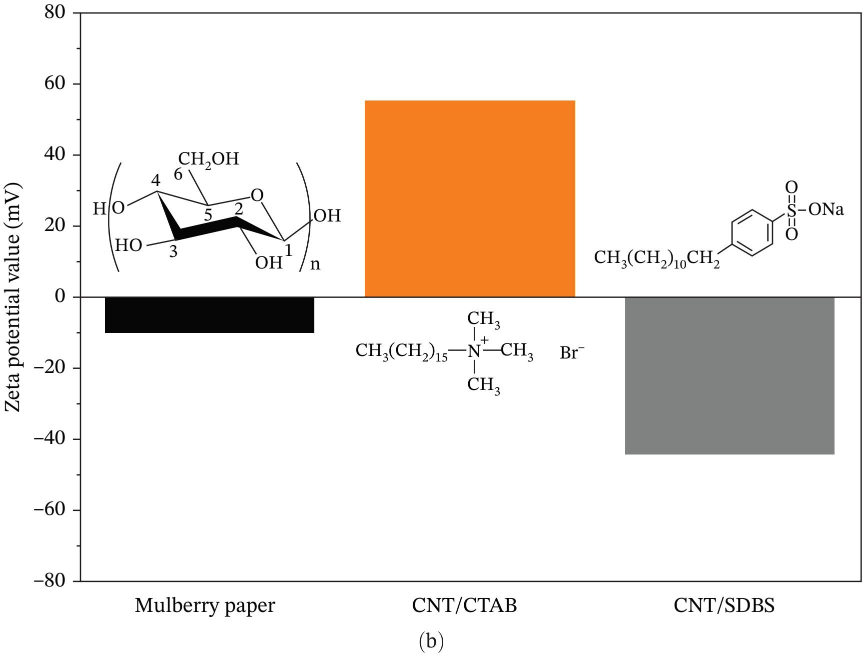

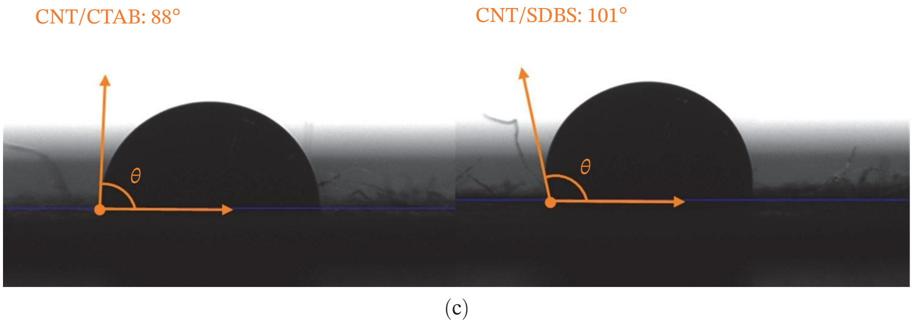

FIGURE 1 | (Continued)

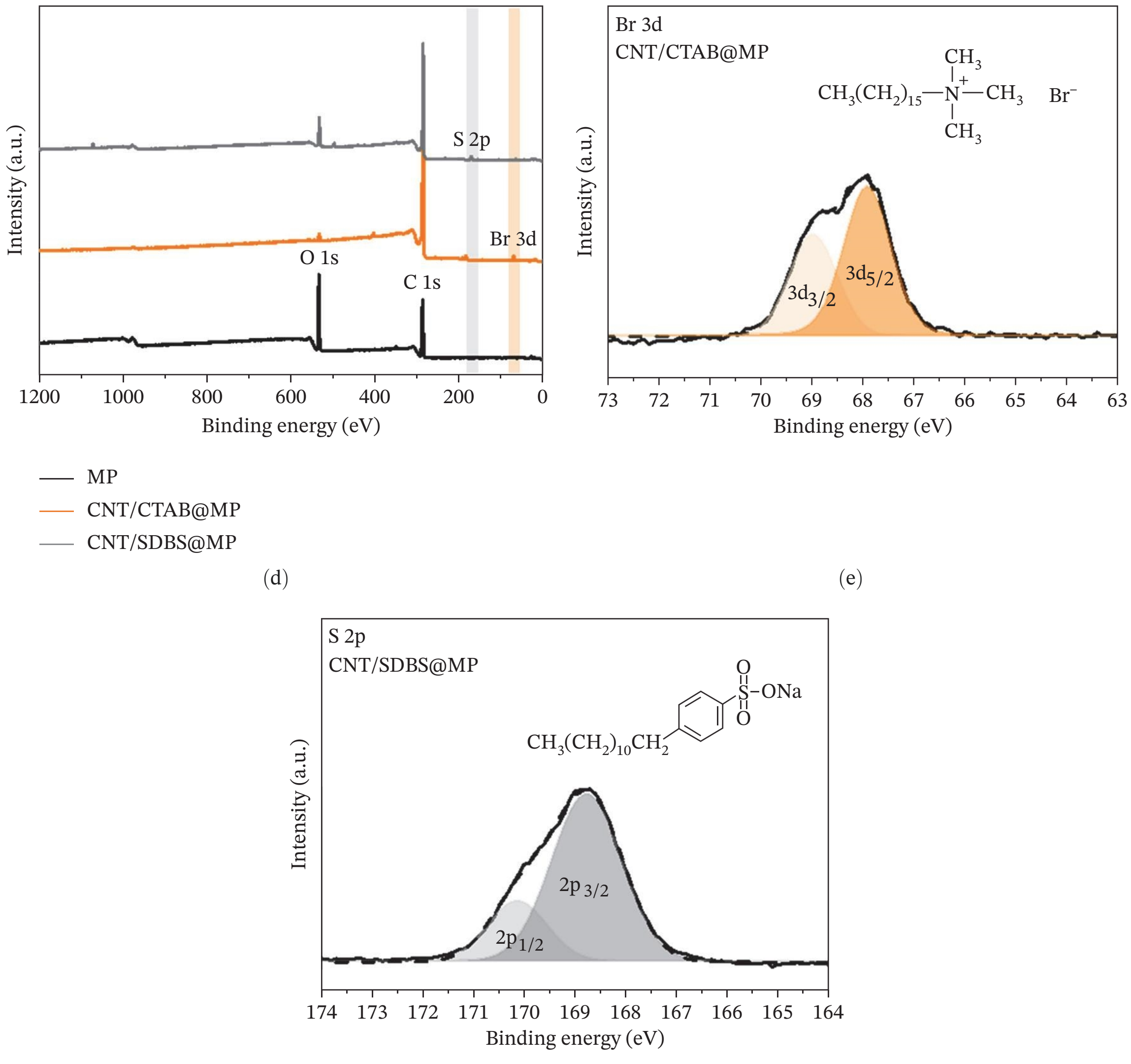

(d)

(e)

(f)

FIGURE 1 | (a) Fabrication process of mulberry paper–based electrodes composed of CNT and PEDOT:PSS as active materials. (b) Zeta potential values of a mulberry paper, CNT/CTAB, and CNT/SDBS dispersions. (c) Contact angle measurements of CNT/CTAB and CNT/SDBS dispersions on mulberry paper. XPS analysis of the chemical composition: (d) full survey spectra of uncoated, CNT/CTAB–, and CNT/SDBS–coated mulberry papers, (e) Br 3d spectrum of CNT/CTAB–coated mulberry paper, and (f) S 2p spectrum of CNT/SDBS–coated mulberry paper.

have consistently reported quasi-reversible Br^-/Br_2 or Br^-/Br_3^- peaks in similar potential range, accompanied by capacitance enhancement [29–32]. In our CNT/CTAB electrode system, well-distributed Br ions present at the electrode surface can act as redox-active species, providing additional pseudocapacitive contribution. To further clarify the effect of Br ions, we examined the CV tests of CNT/CTAB electrode with different CNT:CTAB mass ratios (1:0.5, 1:1, and 1:2) with scan rates of 5–200 $mV\,s^{-1}$ (Figure S9). For all scan rates, the redox-like peak around approximately 0.8 V becomes more enhanced as the CTAB content increased, which indicates that the Br ions introduced by CTAB contribute to the redox process. Based on these results, the enhanced areal capacitance of CNT/CTAB electrode arises from the synergy of improved electrical conductivity and ion accessibility, and bromide-mediated redox reactions. Long-term cycling tests demonstrate the superior stability of the CNT/CTAB electrode. At 1.0 $mA\,cm^{-2}$, it retains 97.9% of its initial capacitance after 10,000 cycles, compared to 93.5% for CNT/SDBS electrode (Figure 2e). Even at a higher current density of 4.0 $mA\,cm^{-2}$, the CNT/CTAB electrode maintained 98.9% capacitance retention after 80,000 cycles, whereas CNT/SDBS electrode exhibited 91.4% capacitance retention (Figure 2f). To clarify the role of surfactant mediated electrostatic interactions on the long-term cycling stability, we performed SEM analysis and pre- and post-cycling EIS measurements for the CNT/CTAB and CNT/SDBS electrodes after 80,000 cycles at an areal current density of 4 $mA\,cm^{-2}$. The cycled CNT/SDBS electrode showed clear CNT delamination from the surface, exposing the underlying mulberry paper fibers (Figure S10). However, the CNT/CTAB electrode maintained uniform CNT coverage with no observable delamination, demonstrating that the cationic surfactant, CTAB, enhances interfacial adhesion to the negatively charged cellulose fibers through the electrostatic attraction. The pre- and post-EIS results corroborated these morphological observations. The R_{ct} of the CNT/CTAB electrode remained nearly constant from the initial (14.0 Ω) to 80,000th cycle (14.7 Ω), whereas that of CNT/SDBS

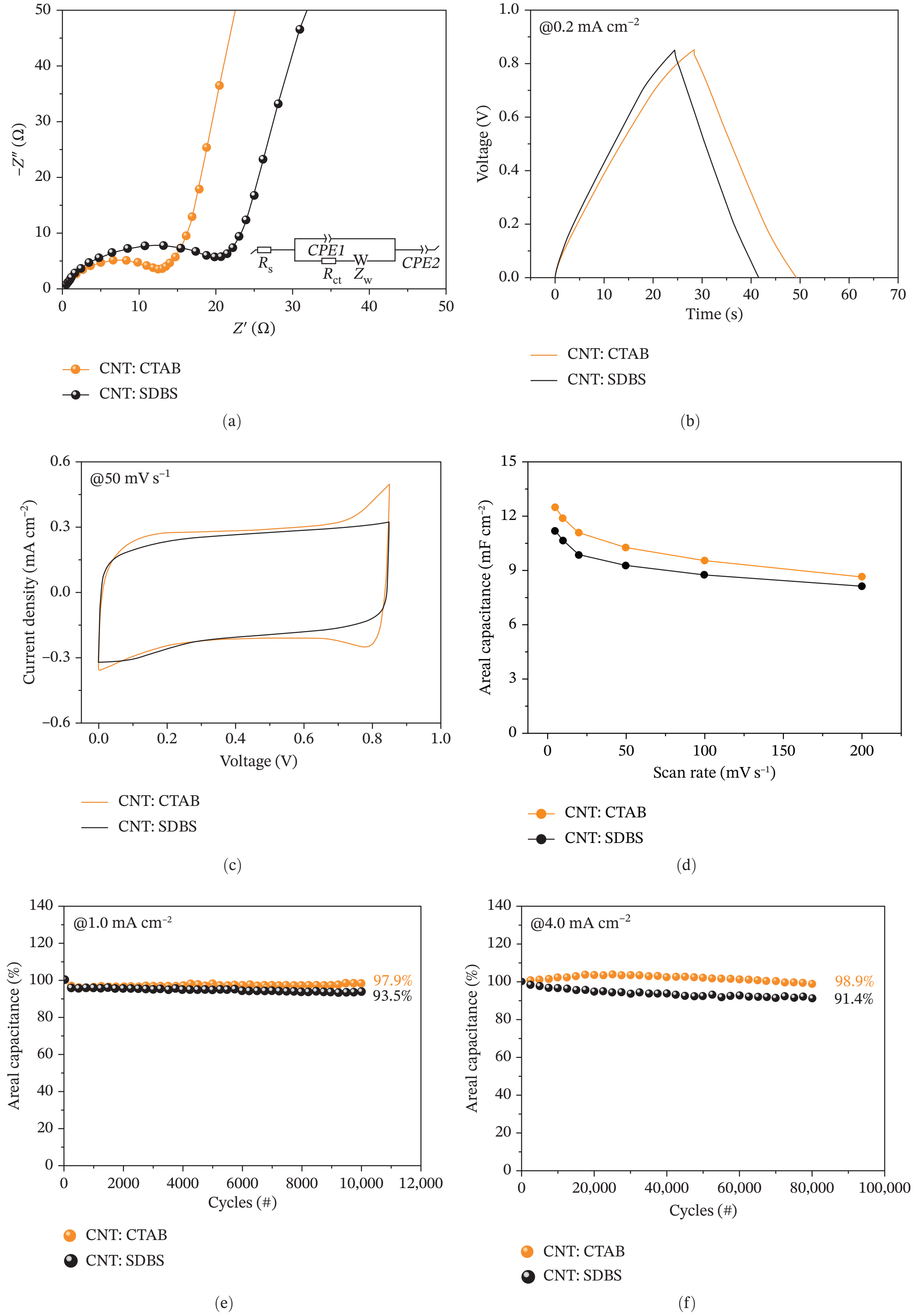

FIGURE 2 | Electrochemical characterization of CNT/CTAB– and CNT/SDBS–coated mulberry paper–based supercapacitors. (a) Nyquist plot with fitted equivalent circuit, (b) GCD profiles at an areal current density of 0.2 mA cm^{-2}. (c) CV curves at a scan rate of 50 mV s^{-1}. (d) Areal capacitances as a function of scan rate (5–200 mV s^{-1}). Long-term cycling stability at areal current densities of (e) 1.0 and (f) 4.0 mA cm^{-2}.

electrode increased from 19.5 to 21.5 Ω (Figure S11). The strengthened binding and robust network formation between CNT/CTAB and the cellulose substrate, driven by the electrostatic attraction, effectively suppress delamination and degradation during extended cycling.

To enhance the energy storage capacity of the CNT/CTAB–coated mulberry paper electrode, we introduced PEDOT:PSS as a pseudocapacitive layer. Given that CNT/CTAB electrode already demonstrated superior electrochemical performance and stability, it served as the optimal electrode for subsequent PEDOT:PSS deposition. However, pristine PEDOT:PSS films often suffer from instability in aqueous environments due to the hydrophilic nature of PSS chains, leading to delamination and capacitance fading [33, 34]. To mitigate this issue, we introduced cross-linking agents—DVS and EG—which can chemically interact with PSS chains via covalent bonding and hydrogen bonding, respectively. Additionally, both agents can act as secondary dopants that modulate the PSS-to-PEDOT ratio, thereby improving electrical conductivity and film robustness. We fabricated three types of electrodes via dip-coating: pristine PEDOT:PSS (C-PEDOT:PSS), DVS–cross-linked (C-PEDOT:PSS-DVS), and EG-cross-linked (C-PEDOT:PSS-EG) films on CNT/CTAB–modified mulberry paper. Their morphologies were shown in SEM images, which confirmed uniform deposition (Figure S12). Table S3 is a summarization of loading mass of C-PEDOT:PSS, C-PEDOT:PSS-DVS, and C-PEDOT:PSS-EG electrodes. FTIR analysis was performed to verify the successful incorporation of cross-linkers into PEDOT:PSS (Figure 3a). To

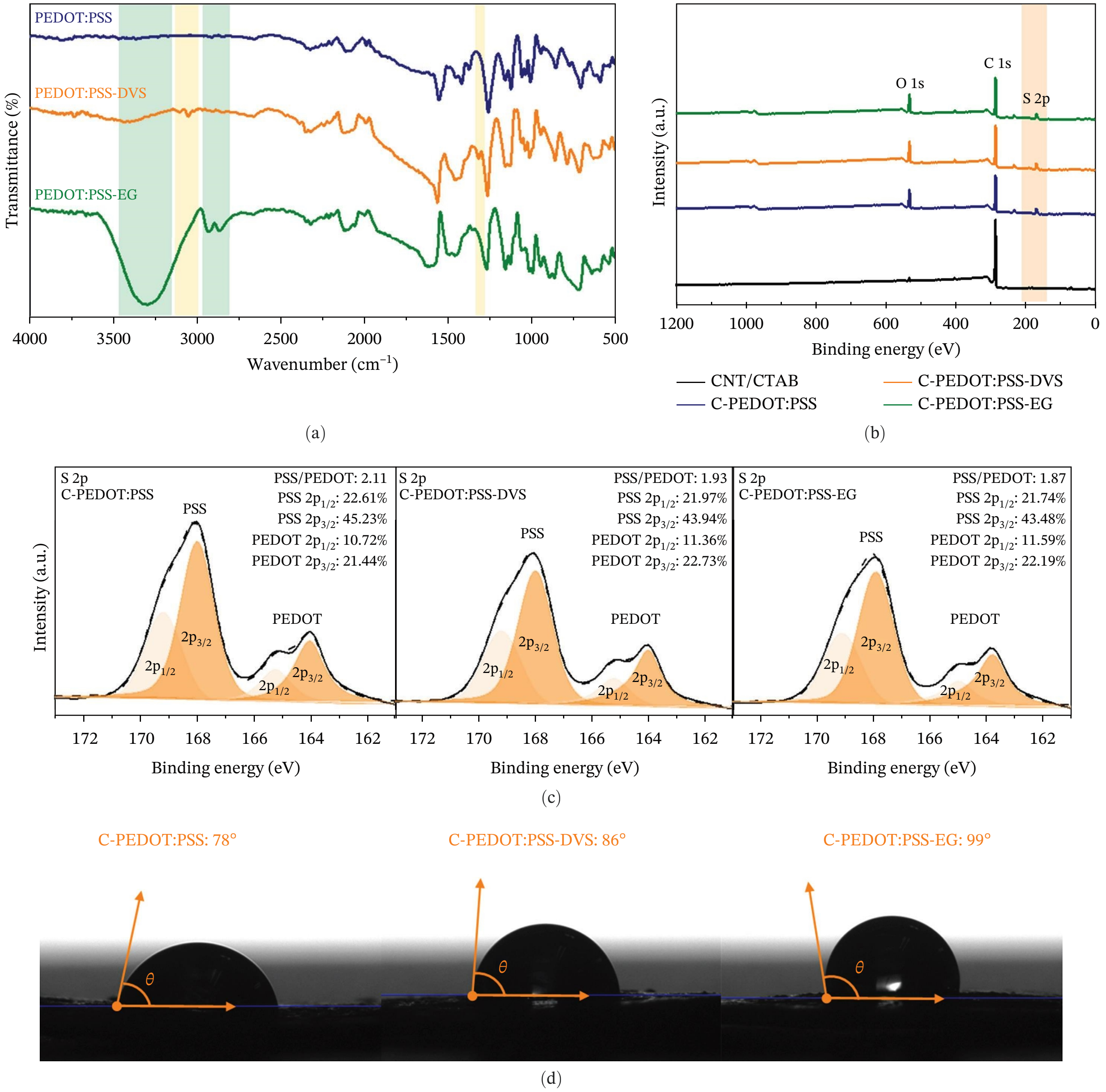

(a)

(b)

(c)

(d)

FIGURE 3 | (a) FTIR spectrum of free standing PEDOT:PSS, PEDOT:PSS-DVS, and PEDOT:PSS-EG films. (b) Full XPS survey result. (c) S 2p peak spectra with PSS and PEDOT area contribution. (d) Contact angle measurements of C-PEDOT:PSS, C-PEDOT:PSS-DVS, and C-PEDOT:PSS-EG electrodes.

identify the specific bonds depending on the cross-linking agents, we conducted FTIR measurements of the free standing PEDOT:PSS, PEDOT:PSS-DVS, and PEDOT:PSS-EG films. New peaks at 3100–3000 and 1310 cm^{-1} in PEDOT:PSS-DVS film are attributed to the vinyl groups (C—CH_2 stretching vibration) and sulfone (OSO) scissoring modes, respectively, confirming covalent cross-linking between PEDOT:PSS and DVS [15, 35]. In PEDOT:PSS-EG film, the broad O—H stretch near 3300 cm^{-1} and C—H vibrations near 2915 and 2853 cm^{-1} suggest hydrogen bonding and EG incorporation [36, 37]. These results indicated that cross-linking reactions of DVS or EG with PEDOT:PSS were successfully achieved. In addition, to clarify the effect of cross-linkers on the mechanical property of PEDOT:PSS–based electrodes, we measured the tensile strength of PEDOT:PSS–based electrodes containing different cross-linkers (DVS and EG; Figure S13). Both C-PEDOT:PSS-DVS and C-PEDOT:PSS-EG electrodes exhibited higher tensile strength (17.5 and 16.2 MPa) than C-PEDOT:PSS electrode (15.6 MPa). This improvement is attributed to the covalent bonding induced by DVS and hydrogen bonding induced by EG, respectively. XPS spectra revealed that the S 2p signal corresponding to PSS (high binding energy) and PEDOT (low binding energy) [38]. To clarify the secondary doping effect of cross-linkers (DVS and EG), we quantify PSS and PEDOT area contributions by fitting symmetric/asymmetric Gaussian–Lorentzian functions over the 161–173 eV range to calculate the PSS-to-PEDOT ratio (Figure 3b,c). Table S4 is a summary of the quantified PSS and PEDOT area, and PSS/PEDOT ratio of C-PEDOT:PSS, C-PEDOT:PSS-DVS, and C-PEDOT:PSS-EG electrodes. The PSS/PEDOT ratio decreased from 2.11 in C-PEDOT:PSS electrode to 1.93 in C-PEDOT:PSS-DVS electrode and 1.87 in C-PEDOT:PSS-EG electrode. These reductions confirm partial removal or suppression of excess PSS, consistent with effective secondary doping [16, 39]. As expected, electrical resistance measurements showed improved conductivity in the cross-linked films: 0.16 kΩ for C-PEDOT:PSS, 0.12 kΩ for DVS, and 0.13 kΩ for EG, consistent with the reduced insulating PSS content (Figure S14). Figure 3d represents contact angle measurements using 1 M H_2SO_4 on each electrode, provided further evidence. Since PSS is hydrophilic, samples with lower PSS content exhibited larger contact angles. The increasing trend—C-PEDOT:PSS (78°) < DVS (86°) < EG (99°)—aligns well with the PSS depletion observed in XPS and suggests that cross-linking not only enhances conductivity but also modulates surface wettability.

To examine the impact of PEDOT:PSS and the role of cross-linking agents, we systematically evaluated the electrochemical performance of CNT/CTAB, C-PEDOT:PSS, C-PEDOT:PSS-DVS, and C-PEDOT:PSS-EG electrodes. EIS measurements revealed that the introduction of PEDOT:PSS increased the R_{ct}, compared to the CNT/CTAB electrode (13.2 Ω; Figure S15). This result is attributed to the effect of higher electrical resistance due to additional electrical resistance from the PEDOT:PSS layer. However, for PEDOT:PSS–based electrodes, the C-PEDOT:PSS-DVS electrode exhibited the lowest R_{ct} (41.0 Ω), followed by C-PEDOT:PSS-EG (52.6 Ω) and C-PEDOT:PSS (82.9 Ω). This trend confirms that DVS, functioning as the secondary dopant, enhanced charge transport kinetics through covalent cross-linking and PSS depletion. GCD profiles at an areal current density of 0.2 mA cm^{-2} demonstrated markedly longer discharge times after introducing the pseudocapacitive PEDOT:PSS layer, verifying enhanced energy storage via Faradaic reactions (Figure 4a). Among them, C-PEDOT:PSS-DVS showed the longest discharge time, indicating the most efficient utilization of the PEDOT:PSS layer due to improved charge transfer kinetics. This behavior was consistent across various current densities (Figure S16). CV measurements further supported these findings. At all scan rates from 5 to 200 mV s^{-1}, C-PEDOT:PSS-DVS electrode exhibited the largest enclosed CV area, followed by C-PEDOT:PSS-EG and pristine PEDOT:PSS electrodes, signifying superior energy storage performance (Figure 4b and S17). The extracted areal capacitance showed the same ranking: C-PEDOT:PSS-DVS > C-PEDOT:PSS-EG > C-PEDOT:PSS > CNT/CTAB (Figure 4c). Specifically, at 50 mV s^{-1}, C-PEDOT:PSS-DVS achieved 30.4 mF cm^{-2}, outperforming C-PEDOT:PSS-EG (24.8 mF cm^{-2}), C-PEDOT:PSS (22.1 mF cm^{-2}), and CNT/CTAB (10.3 mF cm^{-2}). The electrochemical behavior was investigated to confirm the effect of the PEDOT:PSS on the pseudocapacitive contribution in energy storage mechanism by a b-value derived from CV curves at various scan rates based on Equation (3).

$$i = av^b \ , \tag{3}$$

where v is the scan rate, i accounts for the peak current, and b is the electrochemical behavior. A b-value approaching 1.0 indicates capacitive-controlled behavior, while values nearing 0.5 suggests diffusion-controlled behavior. The CNT/CTAB electrode exhibited the b-value of 0.78, whereas C-PEDOT:PSS, C-PEDOT:PSS-DVS, and C-PEDOT:PSS-EG electrodes showed the b-value of 0.75, 0.72, and 0.73, respectively (Figure 4c). Compared to the CNT/CTAB electrode, the lower b-values for PEDOT:PSS–based electrodes confirmed the pseudocapacitive contributions from reversible reduction/oxidation of PEDOT backbone in H_2SO_4 electrolyte, as described by the followed reaction [40]. Moreover, after applying cross-linking agents of DVS or EG to PEDO:TPSS, the pseudocapacitive reaction of C-PEDOT:PSS-DVS and C-PEDOT:PSS-EG electrodes enhanced.

$$\mathrm{PEDOT^+ \cdot PSS^- + H^+ + e^- \leftrightarrow PEDOT^0 \cdot PSS^- \cdot H^+}.$$

Additionally, we quantified the capacitance contribution ratio based on Equation (4).

$$i(v) = k_1 v + k_2 v^{0.5} \ , \tag{4}$$

where the term $k_1 v$ accounts for the capacitive-controlled behavior and $k_2 v^{0.5}$ term is for diffusion-controlled behavior. At a scan rate of 50 mV s^{-1}, the contribution ratio of capacitive-controlled behavior decreased after adding PEDOT:PSS to CNT/CTAB electrode. Based on the calculated percentages of each electrode, the C-PEDOT:PSS-DVS exhibited the lowest capacitive-controlled behavior (42.5%), whereas that of CNT/CTAB, C-PEDOT:PSS, and C-PEDOT:PSS-EG electrodes were 63.7%, 49.6%, and 45.7%, respectively. These results confirmed that the PEDOT:PSS contributed the pseudocapacitance, explaining the highest area capacitance of C-PEDOT:PSS-DVS electrode (Figure S18).

To evaluate long-term durability, cycling tests were conducted at two current densities. After 6000 cycles at 1.0 mA cm^{-2}, the capacitance retentions were 94.0% for C-PEDOT:PSS-DVS, 90.4% for C-PEDOT:PSS-EG, and 85.7% for C-PEDOT:PSS (Figure 4d). At a higher current density of 4.0 mA cm^{-2} over 80,000 cycles (Figure 4e), C-PEDOT:PSS-DVS again outperformed with 95.9% retention, followed by C-PEDOT:PSS-EG (92.8%) and pristine PEDOT:PSS (91.4%). To clarify the origin of the capacitance decay

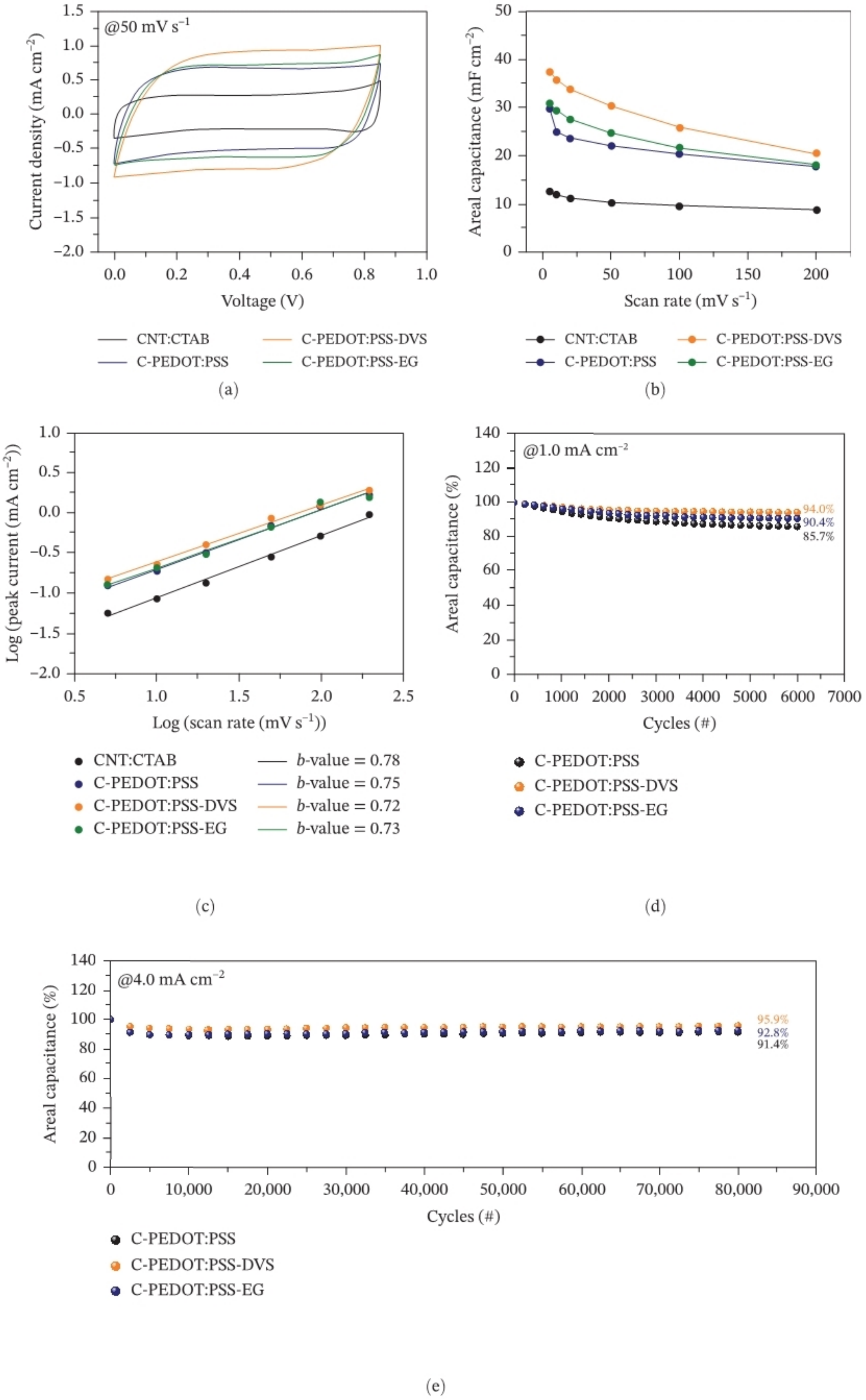

FIGURE 4 | Electrochemical characterization of the CNT/CTAB, C-PEDOT:PSS, C-PEDOT:PSS-DVS, and C-PEDOT:PSS-EG electrodes. (a) CV curves at a scan rate of 50 mV s^{-1}. (b) Areal capacitance at various scan rates from 5 to 200 mV s^{-1}. (c) Relationship between log(scan rate) and log (current density) based on the CV curves. Long-term cycling stabilities of C-PEDOT:PSS, C-PEDOT:PSS-DVS, and C-PEDOT:PSS-EG electrodes at areal current densities of (d) 1.0 and (e) 4.0 mA cm^{-2}.

of the electrodes during long-term cycling, we performed SEM measurements and the pre- and post-cycling EIS measurements for the C-PEDOT:PSS, C-PEDOT:PSS-DVS, and C-PEDOT:PSS-EG electrodes after 80,000 cycles at a current density of 4.0 mA cm^{-2}. As shown in Figure S19, the cycled C-PEDOT:PSS electrode exhibited severe delamination of PEDOT:PSS layer, leading to exposure of the underlying CNT network. In contrast, the cycled C-PEDOT:PSS-DVS electrode remained uniformly covered by the PEDOT:PSS layer even after 80,000 cycling process, demonstrating that DVS effectively suppressed the delamination of PEDOT:PSS and contributed to higher cycling stability. The C-PEDOT:PSS-EG electrode showed intermediate behavior, with partial delamination of PEDOT:PSS coating layer but less severe than C-PEDOT:PSS. Those observations suggest that the strong covalent cross-linking provided by DVS enhances the mechanical integrity and reliability of the electrode. Furthermore, as shown in Figure S20, the R_{ct} of the C-PEDOT:PSS-DVS electrode was nearly constant from the initial (40.6 Ω) to the 80,000th cycle (42.0 Ω), whereas that of C-PEDOT:PSS electrode progressively increases from 81.6 to 89.1 Ω, indicating the electrode degradation during repeated charge–discharge cycling. The R_{ct} of C-PEDOT:PSS-EG electrode also increased from 51.3 to 55.2 Ω, which is less than C-PEDOT:PSS electrode and more than C-PEDOT:PSS-DVS electrode. Pre- and post-cycling EIS results were consistent with SEM images. These results demonstrate that cross-linked PEDOT:PSS with DVS and EG significantly improves electrochemical performance and reliability, due to enhanced conductivity, structural stability, and interfacial adhesion. In particular, the covalent cross-linking by DVS provided stronger bonding than the hydrogen bonding by EG, resulting in more robust electrochemical characteristics. The specific capacitance and capacitance retention of C-PEDOT:PSS-DVS electrode were compared with previously reported flexible supercapacitors (Table S5). Compared to the electrochemical performance of previous literature, the C-PEDOT:PSS-DVS electrode exhibited superior performance, highlighting its potential for flexible supercapacitor. These outstanding performances were attributed to the synergistic effect of the electrostatic attraction and covalent bonding induced by CTAB and DVS, respectively. Therefore, the combination of secondary doping and strong interchain linkage is key to realizing high-performance and stable PEDOT:PSS–based supercapacitors.

To enhance the relevance of C-PEDOT:PSS-DVS electrode for practical wearable applications, we conducted the electrochemical characterization of C-PEDOT:PSS-DVS electrode in neutral 1 M Na_2SO_4 electrolyte, instead of acidic 1 M H_2SO_4 electrolyte

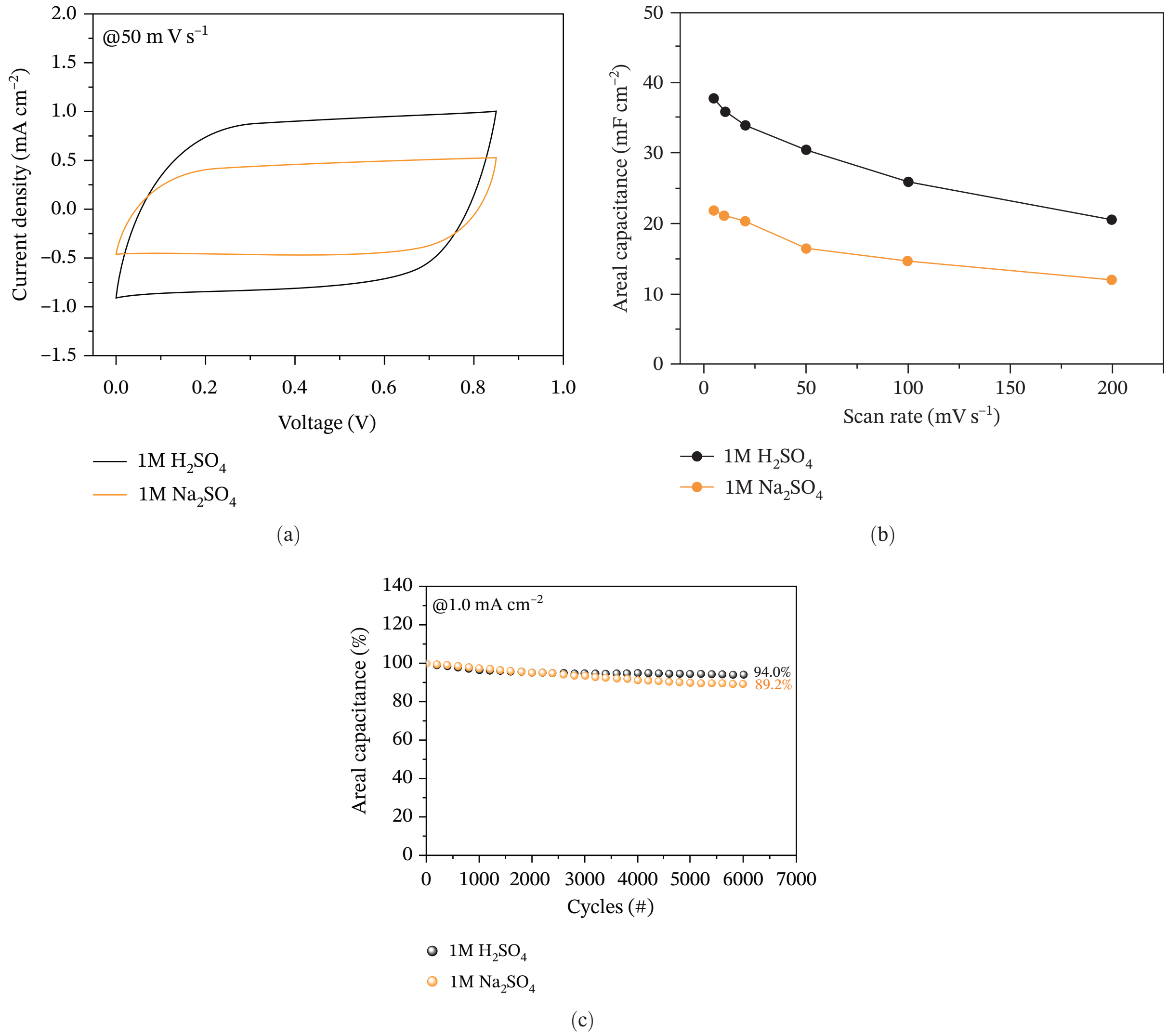

(a)

(b)

(c)

FIGURE 5 | (Continued)

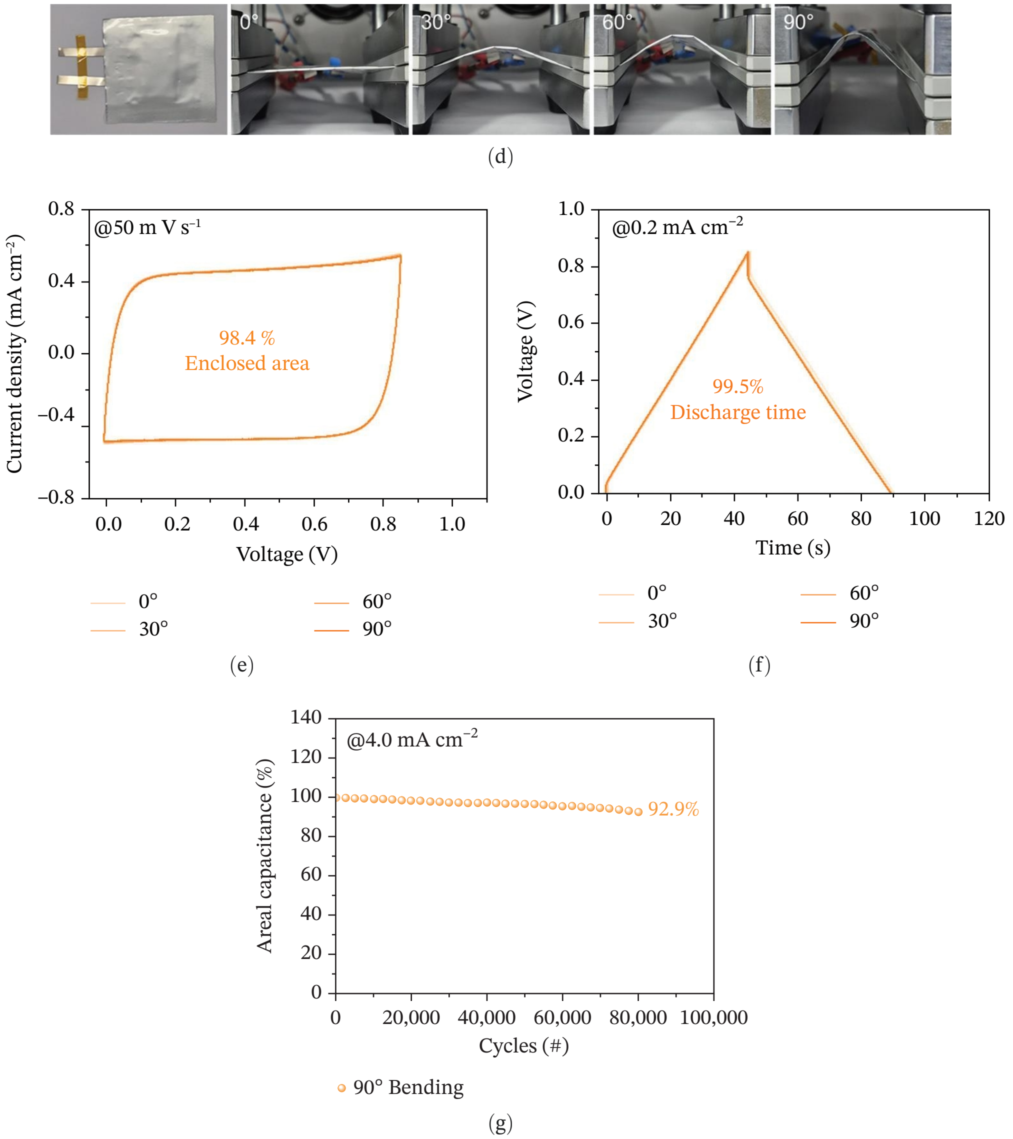

FIGURE 5 | (a) CV curves of C-PEDOT:PSS-DVS electrodes at a scan rate of 50 mV s^{-1} with 1 M H_2SO_4 and 1 M Na_2SO_4 electrolyte. (b) Areal capacitances of C-PEDOT:PSS-DVS electrodes as a function of scan rate (5–200 mV s^{-1}) with 1 M H_2SO_4 and 1 M Na_2SO_4 electrolyte. (c) Long-term cycling stability at an areal current density of 1.0 mA cm^{-2}. (d) Photos of the pouch-type C-PEDOT:PSS-DVS electrode (8 cm^2 active area) and the pouch cell under mechanical bending deformations of 0°, 30°, 60°, and 90°. (e) CV curves of the pouch cell at a scan rate of 50 mV s^{-1} depending on the bending degrees. (f) GCD profiles at an areal current density of 0.2 mA cm^{-2} depending on the bending degrees. (g) Areal capacitance retention under mechanical bending deformation with a degree of 90° of the pouch-type C-PEDOT:PSS-DVS electrode.

(Figure 5a). The enclosed CV area in 1 M Na_2SO_4 electrolyte at a scan rate of 50 mV s^{-1} was smaller than that in 1 M H_2SO_4 electrolyte, indicating that the performance in neutral electrolyte showed lower areal capacitance (Figure 5a). This behavior was consistent across all scan rates from 5 to 200 mV s^{-1} (Figures 5b and S21). Consistently, the GCD profiles in the neutral electrolyte at all current densities showed a shorter discharge time compared to those in the acidic electrolyte (Figure S22). To evaluate long-term durability, cycling test of C-PEDOT:PSS-DVS electrode with different electrolytes was conducted at the areal current density of 1.0 mA cm^{-2} (Figure 5c). After 6000 cycles at 1.0 mA cm^{-2}, the capacitance retentions were 94.0% for 1 M H_2SO_4 electrolyte, and 89.2% for 1 M Na_2SO_4 electrolyte. Based on these results, the poorer electrochemical performance in 1 M Na_2SO_4 compared to 1 M H_2SO_4 was ascribed to lower ion mobility and larger effective size of Na^+ ions, which reduce charge transfer kinetics and induce the structural stress during repeated charge–discharge process [41]. However, for practical wearable supercapacitors, the neutral Na_2SO_4 electrolyte is more appropriate than the acidic 1 M H_2SO_4 electrolyte because the neutral electrolyte offers the biocompatibility, noncorrosiveness, and operational safety. Finally, we demonstrated a large-scale fabrication and mechanical stability of C-PEDOT:PSS-DVS electrode under various bending degrees. Benefiting from the hydrophilic nature of the mulberry paper and the facile solution-based coating process for active materials, we successfully scaled up the electrode area from 1.13 to 64 cm^2 (Figure S23). Moreover, a pouch-type C-PEDOT:PSS-DVS electrode (8 cm^2 active area) was tested in neutral 1 M Na_2SO_4 electrolyte to evaluate the electrochemical performance under various bending degrees of 0°, 30°, 60°, and 90° (Figure 5d). As shown in Figure 5e, at a scan rate of 50 mV s^{-1}, the CV curves of the pouch cell under various bending angles (0°, 30°, 60°, and 90°) exhibited negligible differences with the enclosed area under 90° bending retaining 98.4% of the flat-state enclosed area. The GCD profiles at an areal current density of 0.2 mA cm^{-2} also remained almost unchanged, showing 99.5% discharge time retention (Figure 5f). Additionally, 90° bent-state C-PEDOT:PSS-DVS–based pouch-type supercapacitor exhibited the areal capacitance retention of 92.9% after 80,000 cycles at an areal current density of 4.0 mA cm^{-2}, demonstrating outstanding mechanical electrochemical stability (Figure 5g). The incorporations of cationic CTAB and crosslinker DVS allowed the C-PEDOT:PSS electrode to retain exceptional electrochemical stability under mechanical bending deformation. Consequently, these results confirmed the suitability of C-PEDOT:PSS-DVS electrode for flexible and wearable applications.

4 | Conclusion

This study demonstrates a scalable and chemically tunable strategy for fabricating high-performance and binder-free supercapacitors on mulberry paper, a sustainable, mechanically robust, and hydrophilic substrate. Electrostatic adhesion of CTAB–modified CNTs to the negatively charged cellulose fibers enabled uniform coatings with reduced interfacial resistance and improved electrolyte wettability, outperforming conventional SDBS–based electrodes in both areal capacitance and cycling stability. PEDOT:PSS was molecularly cross-linked using DVS and EG, enhancing electrical conductivity through secondary doping and reinforcing film integrity via covalent and hydrogen bonding. The optimized C-PEDOT:PSS-DVS electrode delivered an areal capacitance of 30.4 mF cm^{-2} at 50 mV s^{-1}, retaining 95.9% of its capacitance after 80,000 cycles at 4.0 mA cm^{-2}. Furthermore, the C-PEDOT:PSS-DVS electrode exhibited the stable electrochemical performance even under mechanical bending deformation. In particular, C-PEDOT:PSS-DVS–based supercapacitor retained 92.9% of the areal capacitance under 90° bending deformation after 80,000 cycles at 4.0 mA cm^{-2}. This work provides key insights into interface-directed charge transport and polymer stabilization, highlighting the promise of renewable fibrous substrates for next-generation wearable and biodegradable energy storage devices.

Author Contributions

Hyungsub Yoon: conceptualization, formal analysis, investigation, data curation, writing – original draft, visualization.**Noemí Aguiló-Aguayo:** investigation, data curation. **Mathis Mortensen Brette:** data curation, writing – review and editing. **Ho-Jin Lee:** formal analysis, investigation, visualization. **Tung Pham, Ji-Won Jung, and Peter Baumli:** investigation, data curation, writing – review and editing. **Ergang Wang:** supervision, data curation, writing – review and editing. **Tae Gwang Yun and Byungil Hwang:** conceptualization, supervision, data curation, writing – review and editing.

Acknowledgments

This research was supported by the Global Research Development Center (GRDC) Cooperative Hub Program through the National Research Foundation of Korea (NRF) funded by the Ministry of Science and ICT (MSIT) (Grant RS-2023-00257595).

Funding

This research was supported by the Global Research Development Center (GRDC) Cooperative Hub Program through the National Research Foundation of Korea (NRF) funded by the Ministry of Science and ICT (MSIT) (Grant RS-2023-00257595).

Conflicts of Interest

The authors declare no conflicts of interest.

Data Availability Statement

The data that support the findings of this study are available from the corresponding author upon reasonable request.

References

1. H. Yang, S. Li, Y. Wu, et al., “Advances in Flexible Magnetosensitive Materials and Devices for Wearable Electronics,” *Advanced Materials* 36, no. 37 (2024): 2311996.

2. K. Zhang, X. Shi, H. Jiang, et al., “Design and Fabrication of Wearable Electronic Textiles Using Twisted Fiber-Based threads,” *Nature Protocols* 19, no. 5 (2024): 1557–1589.

3. X. Ding, Y. Yu, W. Li, F. Bian, H. Gu, and Y. Zhao, “Multifunctional Carbon Nanotube Hydrogels With on-Demand Removability for Wearable Electronics,” *Nano Today* 54 (2024): 102124.

4. C. Sooyong, C. Chih-Ming, and H. Byungil, “Cu-Cu Mechanical Bonding,” in *3D Integration of the Next Generation Electronic Chips: Interfacial Mechanisms, Surface Engineering, And Emerging Low-Temperature Strategies. Facta Universitatis, Series: Mechanical Engineering, [S.l.]*, 2025, Date Accessed: 23 Mar. 2026, https://casopisi.junis.ni.ac.rs/index.php/FUMechEng/article/view/14015.

5. C. Chunghyun, Q. Nadeem, and H. Byungil, “Mechanically Pressed Polymer-Matrix Composites,” in *3D Structured Filler Networks For Electromagnetic Interference Shielding Application. Facta Universitatis, Series: Mechanical Engineering, [S.l.]*, 2024, Date accessed: 23 Mar. 2026, Available at: https://casopisi.junis.ni.ac.rs/index.php/FUMechEng/article/view/12767.

6. B. Yao, J. Zhang, T. Kou, Y. Song, T. Liu, and Y. Li, “Paper-Based Electrodes for Flexible Energy Storage Devices,” *Advanced Science* 4, no. 7 (2017): 1700107.

7. A. Sumboja, J. Liu, W. G. Zheng, Y. Zong, H. Zhang, and Z. Liu, “Electrochemical Energy Storage Devices for Wearable Technology: A Rationale for Materials Selection and Cell Design,” *Chemical Society Reviews* 47, no. 15 (2018): 5919–5945.

8. H. He, G. Huang, X. Yan, et al., “Synergistic Optimization of Polypyrrole/Mulberry Paper-Based Composite Electrode by Carbon Black and Multi-Walled Carbon Nanotubes for High-Performance Flexible All-Solid-State Supercapacitors,” *Journal of Energy Storage* 120 (2025): 116475.

9. Y.-J. Heo, J. W. Lee, Y.-R. Son, et al., “Large-Scale Conductive Yarns Based on Twistable Korean Traditional Paper (Hanji) for Supercapacitor Applications: Toward High-Performance Paper Supercapacitors,” *Advanced Energy Materials* 8, no. 27 (2018): 1801854.

10. T. G. Yun, D. Kim, S.-M. Kim, I.-D. Kim, S. Hyun, and S. M. Han, “Mulberry Paper-Based Supercapacitor Exhibiting High Mechanical and Chemical Toughness for Large-Scale Energy Storage Applications,” *Advanced Energy Materials* 8, no. 21 (2018): 1800064.

11. Y. Han, H. Ha, T. Suryaprabha, P. Baumli, and B. Hwang, “Mulberry-Paper-Based Electrodes With Hybrid Nanocomposite Coatings and Their Application to Eco-Friendly Energy-Storage Devices,” *Cellulose* 31, no. 3 (2024): 1675–1685.

12. M. Pal and K. M. Subhedar, “Facile and Nondestructive Transformation of Intrinsic Hydrophobic Behavior of a Carbon Nanotubes Sheet to

Hydrophilic," *ACS Applied Materials & Interfaces* 16, no. 10 (2024): 13335–13345.

13. Y. Liu, S. Zhang, L. Li, and N. Li, "High-Performance Cellulose Nanofibers/Carbon Nanotubes Composite for Constructing Multifunctional Sensors and Wearable Electronics," *Advanced Fiber Materials* 6, no. 3 (2024): 758–771.

14. J.-S. Jang, Y. Lim, H. Shin, J. Kim, and T. G. Yun, "Bidirectional Water-Stream Behavior on a Multifunctional Membrane for Simultaneous Energy Generation and Water Purification," *Advanced Materials* 35, no. 7 (2023): 2209076.

15. P. J. Bora, A. G. Anil, K. J. Vinoy, and P. C. Ramamurthy, "Outstanding Absolute Electromagnetic Interference Shielding Effectiveness of Cross-Linked PEDOT: PSS Film," *Advanced Materials Interfaces* 6, no. 22 (2019): 1901353.

16. F. Alshabouna, H. S. Lee, G. Barandun, et al., "PEDOT: PSS-Modified Cotton Conductive thread for Mass Manufacturing of Textile-Based Electrical Wearable Sensors by Computerized Embroidery," *Materials Today* 59 (2022): 56–67.

17. V. Ribitsch, K. Stana-Kleinschek, and S. Jeler, "The Influence of Classical and Enzymatic Treatment on the Surface Charge of Cellulose Fibres," *Colloid & Polymer Science* 274, no. 4 (1996): 388–394.

18. Y. Fang, J. G. Hester, B. M. deGlee, et al., "A Novel, Facile, Layer-by-Layer Substrate Surface Modification for the Fabrication of All-Inkjet-Printed Flexible Electronic Devices on Kapton," *Journal of Materials Chemistry C* 4, no. 29 (2016): 7052–7060.

19. Y. Fang and M. M. Tentzeris, "Surface Modification of Polyimide Films for Inkjet-Printing of Flexible Electronic Devices," in *Flexible Electronics*, (IntechOpen, 2018).

20. H. Ha, S. Müller, R.-P. Baumann, and B. Hwang, "Peakforce Quantitative Nanomechanical Mapping for Surface Energy Characterization on the Nanoscale: A Mini-Review," *Facta Universitatis* 22, no. 1 (2024): 1–12, 2024, .

21. H. Ha, S. Mueller, S. Guriyanova, and B. Hwang, "Surface Energy Characterization of a Single Microsphere Particle Using Peakforce Quantitative Nanomechanical Mapping Mode of Atomic Force Microscope," *Facta Universitatis* 23, no. 1 (2025): 171–181.

22. P. Zhu, Y. Kuang, Y. Wei, et al., "Electrostatic Self-Assembly Enabled Flexible Paper-Based Humidity Sensor With High Sensitivity and Superior Durability," *Chemical Engineering Journal* 404 (2021): 127105.

23. J. Khan and M. Mariatti, "Effect of Natural Surfactant on the Performance of Reduced Graphene Oxide Conductive Ink," *Journal of Cleaner Production* 376 (2022): 134254.

24. Y. Htwe and M. Mariatti, "Surfactant-Assisted Water-Based Graphene Conductive Inks for Flexible Electronic Applications," *Journal of the Taiwan Institute of Chemical Engineers* 125 (2021): 402–412.

25. Y. Htwe, M. Abdullah, and M. Mariatti, "Effect of Sodium Dodecyl Concentration on the Properties of Graphene Conductive Inks," *Materials Today: Proceedings* 66 (2022): 2836–2839.

26. Y. Zhao, Y. Tang, X. Wang, and T. Lin, "Superhydrophobic Cotton Fabric Fabricated by Electrostatic Assembly of Silica Nanoparticles and Its Remarkable Buoyancy," *Applied Surface Science* 256, no. 22 (2010): 6736–6742.

27. L. Zhao, Y. Li, M. Yu, Y. Peng, and F. Ran, "Electrolyte-Wettability Issues and Challenges of Electrode Materials in Electrochemical Energy Storage, Energy Conversion, and Beyond," *Advanced Science* 10, no. 17 (2023): 2300283.

28. J. Zhao, H. Lai, Z. Lyu, et al., "Hydrophilic Hierarchical Nitrogen-Doped Carbon Nanocages for Ultrahigh Supercapacitive Performance," *Advanced Materials* 27, no. 23 (2015): 3541–3545.

29. M. Maher, S. Hassan, K. Shoueir, B. Yousif, and M. E. A. Abo-Elsoud, "Activated Carbon Electrode With Promising Specific Capacitance Based on Potassium Bromide Redox Additive Electrolyte for Supercapacitor Application," *Journal of Materials Research and Technology* 11 (2021): 1232–1244.

30. L. Pang and H. Wang, "Inorganic Aqueous Anionic Redox Liquid Electrolyte for Supercapacitors," *Advanced Materials Technologies* 7, no. 4 (2022): 2100501.

31. X. Tang, Y. H. Lui, B. Chen, and S. Hu, "Functionalized Carbon Nanotube Based Hybrid Electrochemical Capacitors Using Neutral Bromide Redox-Active Electrolyte for Enhancing Energy Density," *Journal of Power Sources* 352 (2017): 118–126.

32. L. Li, Y. Wang, J. Meng, et al., "Boosting the Capacitance of MOF-Derived Carbon-Based Supercapacitors by Redox-Active Bromide Ions," *Chemical Engineering Journal Advances* 14 (2023): 100484.

33. X. Fan, W. Nie, H. Tsai, et al., "PEDOT: PSS for Flexible and Stretchable Electronics: Modifications, Strategies, and Applications," *Advanced Science* 6, no. 19 (2019): 1900813.

34. H. Yoon, H. Ha, M. Hong, et al., "Wearable PEDOT: PSS/DVS-Coated Yarn-Type Transpiration-Driven Electrokinetic Power Generator With High Power Efficiency and Water Stability," *Advanced Science* 12, no. 35 (2025): e04463.

35. J. A. Del Olmo, J. M. Alonso, V. S. Martínez, et al., "Biocompatible Hyaluronic Acid-Divinyl Sulfone Injectable Hydrogels for Sustained Drug Release With Enhanced Antibacterial Properties Against *Staphylococcus aureus*," *Materials Science and Engineering: C* 125 (2021): 112102.

36. J.-C. Tsai, Y.-L. Lo, C.-Y. Lin, H.-M. Sheu, and J.-C. Lin, "Feasibility of Rapid Quantitation of Stratum Corneum Lipid Content by Fourier Transform Infrared Spectrometry," *Journal of Spectroscopy* 18, no. 3 (2004): 423–431.

37. W. Wu, H. Zeng, Y. Li, et al., "Structural-Induced Effects of DES in PEDOT: PSS Aqueous Polymerization," *Polymer Testing* 129 (2023): 108272.

38. S.-M. Kim, C.-H. Kim, Y. Kim, et al., "Influence of PEDOT: PSS Crystallinity and Composition on Electrochemical Transistor Performance and Long-Term Stability," *Nature Communications* 9, no. 1 (2018): 3858.

39. A. X. Chen, G. L. Esparza, I. Simon, et al., "Effect of Additives on the Surface Morphology, Energetics, and Contact Resistance of PEDOT: PSS," *ACS Applied Materials & Interfaces* 15, no. 31 (2023): 38143–38153.

40. Y. Fan, T. Wang, R. Asrosa, et al., "Synergistic Contribution of Activated Carbon and PEDOT: PSS in Hybrid Electrodes for High-Performance Planar Micro-Supercapacitors," *Chemical Engineering Journal* 488 (2024): 150672.

41. M. Oneeb, J. Iqbal, A. Mumtaz, et al., "Exploring Electrolyte-Induced Phenomena in Graphene Nanoplatelet-Based Electrodes," *Journal of Electronic Materials* 54, no. 1 (2025): 462–472.

Supporting Information

Additional supporting information can be found online in the Supporting Information section. (*Supporting Information*)

Figure S1 shows the zeta potential vs. pH of the mulberry paper. Figure S2 exhibits the loading mass and electrical resistance of CNT/CTAB and CNT/SDBS electrodes depending on coating cycles. Figure S3 shows SEM images of (a, b) a mulberry paper, (c) CNT/CTAB electrode, and (d) CNT/SDBS electrode. Figure S4 displays EDS elemental mapping images of (a) CNT/CTAB electrode and (b) CNT/SDBS electrode. Figure S5 shows tensile stress–strain curves of mulberry paper, CNT/CTAB, and CNT/SDBS electrodes. Figure S6 shows contact angle measurements of CNT/CTAB and CNT/SDBS electrodes by dropping 1 M H_2SO_4 electrolyte. Figures S7 and S8 are GCD and CV curves of CNT/CTAB and CNT/SDBS electrodes, respectively. Figure S9 is CV curves of CNT/CTAB electrodes with different CNT:CTAB mass ratios (1:0.5, 1:1, and 1:2) with scan rates of 5, 10, 20, 50, 100, and 200 $mV\ s^{-1}$. Figure S10 is SEM images of CNT/CTAB and CNT/SDBS electrodes after 80,000 charge–discharge cycles at a current density of 4.0 $mA\ cm^{-2}$. Figure S11 shows pre- and post-cycling EIS analysis of (a) CNT/CTAB and (b) CNT/SDBS electrodes. Figure S12 shows SEM images of C-PEDOT:PSS, C-PEDOT:PSS-DVS, and C-PEDOT:PSS-EG electrodes. Figure S13 is tensile stress–strain curves of C-PEDOT:PSS, C-PEDOT:PSS-DVS, and C-PEDOT:PSS-EG electrodes. Figure S14 is the electrical resistance of C-PEDOT:PSS, C-PEDOT:PSS-DVS, and C-PEDOT:PSS-EG electrodes. Figure S15 exhibits Nyquist plot of CNT/CTAB, C-PEDOT:PSS, C-PEDOT:PSS-DVS, and C-PEDOT:PSS-EG electrodes with fitted equivalent circuit. Figures S16 and S17 show GCD and CV curves of C-PEDOT:PSS, C-PEDOT:PSS-DVS, and C-PEDOT:PSS-EG electrodes, respectively. Figure S18 exhibits the contribution ratios of electrochemical behavior of CNT/CTAB, C-PEDOT:PSS, C-PEDOT:PSS-DVS, and C-PEDOT:PSS-EG electrodes at a scan rate of 50 $mV\ s^{-1}$. Figure S19 shows SEM images of C-PEDOT:PSS, C-PEDOT:PSS-DVS, and C-PEDOT:PSS-EG electrodes after 80,000 charge–discharge cycles at a current density of 4.0 $mA\ cm^{-2}$. Figure S20 describes pre- and post-cycling EIS analysis of (a) C-PEDOT:PSS, (b) C-PEDOT:PSS-DVS, and (c) C-PEDOT:PSS-EG electrodes. Figures S21 and S22 are CV curves and GCD curves of C-PEDOT:PSS-DVS electrodes with different electrolyte types of 1 M H_2SO_4 and 1 M Na_2SO_4, respectively. Figure S23 depicts images of large scalability of C-PEDOT:PSS-DVS with the active area from 1.13 to 64 cm^2. Table S1 exhibits the zeta potential data of mulberry paper at various pH values. Table S2 is the summary of loading mass and electrical resistance of CNT/CTAB and CNT/SDBS electrodes depending on coating cycles. Table S3 is the summary of loading mass of C-PEDOT:PSS, C-PEDOT:PSS-DVS, and C-PEDOT:PSS-EG electrodes. Table S4 is the summary of PSS and PEDOT area, and PSS/PEDOT ratio of the C-PEDOT:PSS, C-PEDOT:PSS-DVS, and C-PEDOT:PSS-EG electrodes based on XPS results. Table S5 is the comparison of the specific capacitance and capacitance retention of the flexible supercapacitors.